Set-Oriented and Finite-Element Study of Coherent Behavior in Rayleigh-Bénard Convection

Anna Klünker[1], Christiane Schneide[1], Gary Froyland[2], Jörg Schumacher[3], and Kathrin Padberg-Gehle[1(✉)]

[1] Institute of Mathematics and its Didactics, Leuphana Universität Lüneburg, Universitätsallee 1, 21335 Lüneburg, Germany
{anna.kluenker,christiane.schneide,padberg}@leuphana.de
[2] School of Mathematics and Statistics, University of New South Wales, Sydney, NSW 2052, Australia
g.froyland@unsw.edu.au
[3] Department of Mechanical Engineering, Technische Universität Ilmenau, P.O. Box 100 565, 98684 Ilmenau, Germany
joerg.schumacher@tu-ilmenau.de

Abstract. Transfer operator methods have been recognized as powerful tools for the computational study of transport and mixing processes in nonautonomous dynamical systems. The main applications in this context have been geophysical flows with large-scale and long-lived isolated vortical coherent flow structures such as eddies or gyres. The present paper aims to demonstrate the applicability of set-oriented and finite-element frameworks to more complex systems. To this end, we study coherent behavior in turbulent Rayleigh-Bénard convection in two- and three-dimensional settings.

1 Introduction

Transport and mixing processes have been widely studied in dynamical systems. Of key interest are regions in the phase space of an autonomous or a nonautonomous dynamical system that remain coherent, or minimally dispersive, under the action of the flow. Over the last two decades, a number of different concepts have been proposed that describe the notion of Lagrangian coherent behavior. For discussions and comparisons of the major current approaches we refer to [1,2].

Among these established concepts are transfer operator-based methods within a set-oriented numerical framework. Similar in spirit to cell-mapping techniques [3,4], Dellnitz and Hohmann [5] developed a set-oriented approach for the outer approximation of attracting sets in dissipative dynamical systems. Dellnitz and Junge [6,7] extended these ideas to approximate natural invariant measures as well as almost-invariant and almost-cyclic sets of the underlying dynamical

O. Junge et al. (Eds.): SON 2020, SSDC 304, pp. 86–108, 2020.
https://doi.org/10.1007/978-3-030-51264-4_4

system. Almost-invariant sets [6,7] and their finite-time counterparts [8,9] are spatially fixed regions in phase space with the property that trajectories leave such a set only with a relatively small probability over a given time span. Hence, almost-invariant sets mitigate transport between their interior and the rest of phase space.

The key mathematical tool for this probabilistic approach is the Perron-Frobenius operator (transfer operator) or, for continuous-time dynamics, its generator [10]. In a set-oriented framework, the Ulam approximation [11] of the transfer operator produces a stochastic matrix and there are many results in the literature, dating back to [12], concerning the convergence of the leading eigenvector of the resulting stochastic matrix to a physical invariant measure (when one exists). Eigenvectors corresponding to real eigenvalues close to one contain information about almost-invariant sets [7]. This latter concept has been applied to many different dynamical systems, including molecular dynamics [13,14], astrodynamics [15,16], and ocean dynamics [17,18]. A special type of (almost-) invariant sets are attracting sets in dissipative systems and their basins, which can also be identified based on leading eigenvectors of the numerical transfer operator [4,19,20] or the generator [21].

The almost-invariant set framework was extended by Froyland and coworkers to the identification of mobile regions that move about with minimal dispersion under the time-asymptotic [22] and finite-time [23–25] action of a nonautonomous dynamical system. In the finite-time setting, subdominant singular vectors of numerically approximated transfer operators are used to determine the phase space structures of interest. The relation between almost-invariant sets and finite-time coherent sets was discussed in [25]. In [26] the existence of coherent sets over long time spans was linked to the existence of almost-invariant sets for small time spans, given that the coherent sets move sufficiently slowly. A study of coherent sets for the Fokker-Planck equation is in [27] and recent generator-based approaches remove the need for trajectory integration in periodically driven [28] and aperiodically driven [29] flows.

The set-oriented approach to identifying finite-time coherent sets relies on the addition of small amount of diffusion to create the necessary spectral gap [24]; in fact this reliance is also present for almost-invariant sets. In practice, this diffusion is usually provided by the numerical diffusion inherent in the set-oriented numerics. By formally sending this added diffusion to zero, one arrives at a second-order differential operator called the dynamic Laplace operator [30]. The dominant eigenfunctions of the dynamic Laplacian correspond to the dominant singular vectors of the transfer operator. A finite-element approach [31] to approximating the dynamic Laplacian provides a robust, numerical scheme for sparse trajectory data. The cluster-based approach [32] for the estimation of finite-time coherent sets from sparse trajectory data with possibly missing trajectory elements has been followed by several other data-based methods [33–36].

Transfer operators can also be employed to estimate finite-time expansive behavior along trajectories in autonomous and nonautonomous dynamical systems. Finite-time entropy (FTE) captures nonlinear stretching directly from the entropy growth experienced by a small localized density evolved by the transfer

operator. An approximation of the FTE field can be obtained very efficiently within the set-oriented framework. It gives very similar results to finite-time Lyapunov exponent [37] calculations, which many of the geometric approaches for the identification of Lagrangian coherent structures are based on [38]. The FTE-concept has been introduced in [39], see also [40] for related previous work.

In this chapter we consider Rayleigh–Bénard convection (RBC), which is an idealized model of thermal convection in natural systems. In RBC a fluid layer placed between two solid horizontal plates is uniformly heated from below and cooled from above [41]. This model setting contains already many of the properties which can be observed in natural convection flows. One is the formation of large-scale coherent patterns when RBC is investigated in horizontally extended domains [42–47]. These coherent sets, which have been detected in the Eulerian frame of reference, are termed turbulent superstructures as the characteristic horizontal scale extends the height of the convection layer. In thermal convection flows, they consist of convection rolls and cells that are concealed in instantaneous velocity fields by turbulent fluctuations. However, they show up prominently after time averaging of the velocity or temperature fields.

In this paper, we will extend our previous Lagrangian investigations of coherent behavior in turbulent Rayleigh-Bénard convection flows [48,49]. We begin by discussing transport phenomena in nonautonomous systems and the transfer operator framework for the identification of coherent flow behavior in Sect. 2. In Sect. 3 the numerical approximation of such operators within a set-oriented approach is described, and in Sect. 4 the finite-element approach is outlined. The discretized transfer operator and dynamic Laplace operator are the fundamental tools for the extraction of coherent sets and transport barriers and we will introduce the respective approaches. In Sect. 5 we will apply these methods to turbulent Rayleigh-Bénard convection flows in two and three dimensions. In particular, we will extract turbulent superstructures of convection in terms of dominant convection roles. We conclude with a short discussion and outlook in Sect. 6.

2 Nonautonomous Dynamics, Transfer Operators and Transport

We consider a nonautonomous differential equation

$$\dot{\mathbf{x}} = \mathbf{u}(\mathbf{x}, t) \tag{1}$$

with state $\mathbf{x} \in M \subset \mathbb{R}^d$, time $t \in \mathbb{R}$ and sufficiently smooth right-hand side $\mathbf{u}$ such that the flow map $\Phi(\mathbf{x}, t; \tau) : M \times \mathbb{R} \times \mathbb{R} \to M$, $M \subset \mathbb{R}^d$ exists. Here τ denotes the flow time and t the initial time. We aim at identifying almost-invariant and coherent subsets of M, i.e. mobile regions in M that minimally mix with the surrounding phase space. Frequently used indicators for barriers of transport and hence boundaries of coherent regions are ridges in the **finite-time Lyapunov exponent** (FTLE) field [37]

$$FTLE(\mathbf{x}, t; \tau) = \frac{1}{2|\tau|} \log \left(\lambda_{max} [D_{\mathbf{x}} \Phi(\mathbf{x}, t; \tau)^\top D_{\mathbf{x}} \Phi(\mathbf{x}, t; \tau)] \right). \tag{2}$$

They are the basis of some geometric approaches for the identification of Lagrangian coherent structures [38]. In this work, we follow a probabilistic approach, which considers the evolution of sets, or, more abstractly, probability measures. Later, when discussing the dynamic Laplacian, we follow a geometric approach related to finding persistently small set boundaries.

A set $A \subset M$ is called **Φ-invariant** over $[t, t+\tau]$ if $\Phi(A, t+s; -s) = A$ for all $0 \leq s \leq \tau$. That is, the set A remains unchanged under the evolution of Φ. Almost-invariant sets obey an approximate invariance principle $\Phi(A, t+s; -s) \approx A$ for all $0 \leq s \leq \tau$. To be more precise, given a probability measure μ on M, we call a set $A \subset M$ with $\mu(A) \neq 0$ **almost-invariant** [6] over $[t, t+\tau]$ if

$$\rho(A) := \frac{\mu(A \cap \Phi(A, t+\tau; -\tau))}{\mu(A)} \approx 1. \tag{3}$$

If $A \subset M$ is almost-invariant over the interval $[t, t+\tau]$, then the probability (according to μ) of a trajectory leaving A at some time in $[t, t+\tau]$ and not returning to A by time $t+\tau$ is relatively small.

Unlike almost-invariant sets, **coherent sets** are allowed to move in phase space under the evolution of the time-dependent system. Given a reference probability measure μ on M at time t, one seeks to find pairs of sets $(A_t, A_{t+\tau})$ [23] such that

$$\rho(A_t, A_{t+\tau}) = \frac{\mu(A_t \cap \Phi(A_{t+\tau}, t+\tau; -\tau))}{\mu(A_t)} \approx 1. \tag{4}$$

Equation (4) measures the proportion of the set A_t at time t that is mapped to the set $A_{t+\tau}$ at time $t+\tau$ and one seeks to find sets such that $A_{t+\tau} \approx \Phi(A_t, t; \tau)$. Under set-oriented discretisation, optimal almost-invariant [8] and coherent [23] sets maximize (3) and (4).

The NP-hard discrete optimization problems can then be approximately solved by considering the Perron-Frobenius operator $\mathbf{P}_{t,\tau} : L^1(M, m) \to L^1(M, m)$ associated with the flow map Φ, where m denotes Lebesgue measure. The transfer operator is defined by

$$\mathbf{P}_{t,\tau} f(\mathbf{x}) = \frac{f(\Phi(\mathbf{x}, t+\tau; -\tau))}{|\det D\Phi(\Phi(\mathbf{x}, t+\tau; -\tau), t; \tau)|} \tag{5}$$

The interpretation is that if f is a density and $f(\mathbf{x})$ the density value in $\mathbf{x}$ at time t, then $\mathbf{P}_{t,\tau} f(\mathbf{x})$ describes the density value in $\Phi(\mathbf{x}, t; \tau)$ at time $t+\tau$ induced by the flow map. In [24,25] it was shown that maximizing ρ in (3) and (4) can be described in the framework of optimizing an inner product involving a compact self-adjoint operator obtained from $\mathbf{P}_{t,\tau}$. In order to avoid the technical functional analytic description underlying [24,25], we will briefly recall the concept of finite-time coherent sets in the finitary setting [23] in Sect. 3.2 based on a finite-rank approximation of $\mathbf{P}_{t,\tau}$ introduced in Sect. 3.1.

A stretching measure, similar to FTLE in (2), has been derived using the evolution of $\mathbf{P}_{t,\tau}$ [39]. It is based on the concept of differential entropy $h(f) = -\int_\Omega f \log f \; dm$, where Ω is the support of the density f. For a given initial

condition $\mathbf{x}_0$, let $f_{\epsilon,\mathbf{x}_0} := \frac{1}{m(B_\epsilon(\mathbf{x}_0))}\mathbf{1}_{B_\epsilon(\mathbf{x}_0)}$ denote a uniform density supported on $B_\epsilon(\mathbf{x}_0)$, a ball of radius ϵ about $\mathbf{x}_0$. An ϵ-smoothing operator is then defined by

$$\mathbf{A}_\epsilon f(\mathbf{x}) := \frac{1}{m(B_\epsilon(\mathbf{x}))}\int_{B_\epsilon(\mathbf{x})} f \; dm.$$

The rate of increase in entropy experienced in the ϵ-neighborhood of $\mathbf{x}_0$ over the time span $[t, t+\tau]$ of the ϵ-perturbed dynamics can now be described by

$$FTE_\epsilon(\mathbf{x}_0, t; \tau) := \frac{1}{|\tau|}[h(\mathbf{A}_\epsilon \mathbf{P}_{t,\tau} f_{\epsilon,\mathbf{x}_0}) - h(f_{\epsilon,\mathbf{x}_0})]. \tag{6}$$

In [39] several properties of FTE_ϵ and its deterministic limit $\lim_{\epsilon\to 0} FTE_\epsilon$ have been derived. In particular, FTE_ϵ measures nonlinear stretching and can be compared with finite-time Lyapunov exponents (2) in the deterministic limit. In Sect. 3.3 we will outline a very efficient set-oriented approximation of the FTE-field.

We denote by $\mathbf{P}_{t,\tau,\epsilon} := \mathbf{A}_\epsilon \mathbf{P}_{t,\tau}\mathbf{A}_\epsilon$ the slightly mollified transfer operator. As mentioned above, finite-time coherent sets are extracted from the dominant singular vectors of the normalised L^2-compact operator $\mathbf{L}_{t,\tau,\epsilon} := \mathbf{P}_{t,\tau,\epsilon}/(\mathbf{P}_{t,\tau,\epsilon}\mathbf{1})$; see [24], also [25].

One could equivalently consider the dominant eigenvectors[1] of $\mathbf{L}^*_{t,\tau,\epsilon}\mathbf{L}_{t,\tau,\epsilon}$, and in the pure advection limit of $\epsilon \to 0$, one obtains

$$\lim_{\epsilon\to 0} \frac{\mathbf{L}^*_{t,\tau,\epsilon}\mathbf{L}_{t,\tau,\epsilon} - I}{\epsilon^2} = \Delta^D_{[t,t+\tau]},$$

where $\Delta^D_{[t,t+\tau]}$ is the dynamic Laplace operator [30], a self-adjoint, elliptic, second-order differential operator.

Extending ideas from isoperimetric theory, which concern sets of minimal boundary size relative to volume (the Cheeger ratio), one can create a *dynamic* isoperimetric theory [30] and prove connections between the spectrum of $\Delta^D_{[t,t+\tau]}$ and sets with persistently small boundary size relative to evolved volume (the dynamic Cheeger ratio). These sets with persistently small boundary size relative to evolved volume are excellent candidates for finite-time coherent sets because their boundaries resist filamentation and in the presence of small diffusion, diffusive flux across the boundary is minimised. In analogy to the second singular value of $\mathbf{L}_{t,\tau,\epsilon}$ bounding the mixing factor over $[t, t+\tau]$ of all nonequilibrium distributions (Theorem 2 [24], Theorems 3 and 4 [25]), the second singular value of $\Delta^D_{[t,t+\tau]}$ bounds the smallest Cheeger ratio taken over all smooth decompositions of the domain (Corollary 3.6 [30]).

3 Set-Oriented Numerical Framework

We now describe a set-oriented numerical framework for the approximation of the nonautonomous Perron-Frobenius operator in terms of a transition matrix

[1] In the following expression $\mathbf{L}^*_{t,\tau,\epsilon}$ is the adjoint of $\mathbf{L}_{t,\tau,\epsilon}$ between its domain and codomain; see [24] for details.

of a finite-state Markov chain. The discretized transfer operator is the basis for extracting coherent sets (Sect. 3.2) as well as for the computation of FTE-fields (Sect. 3.3).

3.1 Approximation of Transfer Operator

Following [23] we consider some compact subset $X \subset M$ and a small neighborhood Y of $\Phi(X, t; \tau)$. Let $\{B_1, \ldots, B_k\}$ be a partition of X, $\{C_1, \ldots, C_n\}$ a partition of Y. The partition elements are typically generalized rectangles, but other settings are possible. Applying Ulam's method [11] a finite-rank approximation of $\mathbf{P}_{t,\tau} : L^1(X, m) \to L^1(Y, m)$ is given via the transition matrix

$$P_{ij} = \frac{m(B_i \cap \Phi(C_j, t+\tau; -\tau))}{m(B_i)},\ i = 1, \ldots, k,\ j = 1, \ldots, n \tag{7}$$

where we drop the t and τ-dependence of P for brevity. In practice the entries P_{ij} of the transition matrix P are estimated via

$$P_{ij} \approx \frac{\#\{r : \Phi(\mathbf{z}_{i,r}, t; \tau) \in C_j\}}{R}. \tag{8}$$

with uniformly distributed sample points $\mathbf{z}_{i,r}, r = 1, \ldots, R$ chosen in each partition element B_i, $i = 1, \ldots, k$. P is a sparse, row-stochastic matrix and thus all its eigenvalues are contained in the unit circle. For the efficient computation of the transition matrix P we use the software package GAIO [50] (available at http://github.com/gaioguy/GAIO).

The interpretation of the P-induced dynamics is that if $\mathbf{p} \geq 0$ (component-wise) is a probability vector ($\sum_i p_i = 1$), then $\mathbf{p}' = \mathbf{p}P$ is the push-forward of $\mathbf{p}$ under the discretized action of $\Phi(\cdot, t; \tau)$. Note that the numerical scheme introduces diffusion – which is also theoretically needed for robust results [24,25].

3.2 Extracting Finite-Time Coherent Sets

Consider a reference probability measure μ on X at time t, which is discretely represented as a probability vector $\mathbf{p}$ with $p_i = \mu(B_i)$, $i = 1, \ldots, k$. The image probability vector on Y at time $t + \tau$ is then simply computed as $\mathbf{q} = \mathbf{p}P$. We assume both $\mathbf{p} > 0$ and $\mathbf{q} > 0$ (component-wise) and form a normalized matrix L via

$$L_{ij} = \frac{p_i P_{ij}}{q_j}. \tag{9}$$

This matrix has the property that $\mathbf{1}_{\mathbb{R}^k} L = \mathbf{1}_{\mathbb{R}^n}$. In [23,24] it was shown that (under some technical assumptions) the problem of finding optimal coherent sets can be approximated by considering the left eigenvectors $\mathbf{w}_2 \in \mathbb{R}^k$ of LL^* and $\hat{\mathbf{w}}_2 \in \mathbb{R}^n$ of L^*L to the second largest eigenvalue $\lambda_2 < 1$. Here $L^* = P^\top$. Note that these two eigenvalue problems can be turned into the task of finding leading singular values and corresponding left and right singular vectors of a sparse

matrix (see [23] for the exact construction), which can be very efficiently computed by iterative schemes (e.g. `svds` in MATLAB). The signed vector entries of $\mathbf{w}_2$ and $\hat{\mathbf{w}}_2$ can be interpreted as relaxations of indicator functions of the sets A_t and $A_{t+\tau}$ and their complements. Thus the vector $\mathbf{w}_2$ defines fuzzy coherent sets on X, whereas $\hat{\mathbf{w}}_2$ represents their image on Y. Optimal partitions of X and Y into finite-time coherent pairs can be approximated via a line search in $\mathbf{w}_2$ and $\hat{\mathbf{w}}_2$ [23,25]. However, this approach is restricted to finding two-partitions in terms of a coherent set and its complement. In practice, there are often $k > 2$ singular values close to one (followed by a spectral gap) whose corresponding singular vectors highlight the location of coherent sets. In this case, one can postprocess the singular vectors by a k-means clustering to obtain a hard partition into k coherent sets. Alternatively, to preserve the eigenspace structure, one can project the singular vectors to a sparse basis (SEBA) [51], where the entries of each vector denote probabilities that the underlying box B_i belongs to a specific coherent set. Hard assignment of boxes to sets may then be performed by thresholding (see [51]) to form (i) a subpartition of unity, (ii) the largest collection of disjoint sets, or (iii) by maximum likelihood.

3.3 Set-Oriented Computation of FTE

In the discrete context, densities (which are central to the FTE-construction in Eq. (6)) are now represented by discrete probability measures μ and the entropy of a probability vector $\mathbf{p}$ with $p_i = \mu(B_i)$, $i = 1, \ldots, k$, is simply $H(\mathbf{p}) = -\sum_{i=1}^{n} p_i \log p_i$. Under the assumption that all partition elements $\{B_1, \ldots, B_k\}$ are of equal volume let δ_i be a k-vector with a 1 in the i^{th} position and 0 elsewhere. Then the discrete FTE of a partition set B_i is given by

$$FTE(B_i, t; \tau) = \frac{1}{|\tau|} H(\delta_i P) = -\frac{1}{|\tau|} \sum_{j=1}^{n} P_{ij} \log P_{ij}. \tag{10}$$

Note that once the transition matrix P has been computed, the FTE field (6) can be very quickly approximated by application of Eq. (10). In particular, we do not require to explicitly push forward probability densities with P. In addition, stretching rates for differing box volumes as well as for the backward-time dynamics can be conveniently computed, see [39] for more details.

4 Finite-Element Framework

A set-oriented approach for approximating $\Delta^{D}_{[t,t+\tau]}$ is possible and effective [30]. The ingredients are Ulam approximation(s) of the dynamics and a finite-difference approximation of the standard Laplace operator. As the dynamic Laplace operator is an elliptic second-order differential operator, it turns out to be more efficient to adapt the well-worn finite-element approximation approach to our dynamic setting [31]. The main advantages are the ability to produce good results with dramatically decreased trajectory numbers, and the increased

smoothness of the estimates (continuous, piecewise-affine approximations rather than the discontinuous, piecewise-constant approximations from Ulam). One of the main advantages of the set-oriented framework, namely sparsity, is retained. The finite-element approach detailed in [31] has other structural benefits, such as preservation of the symmetry of the true operator, and the ability to have incomplete trajectories.

Briefly, in the time interval $[t, t+\tau]$, one creates a sequence of n time instances $t = t_1 < t_2 < \cdots < t_n = t + \tau$ at which one has N trajectory data points $\mathbf{x}_{i,k} := \Phi(\mathbf{x}_i, t; t_k - t)$, $i = 1, \ldots, N$, $k = 1, \ldots, n$. At the time instance t_k, the trajectory points are meshed and a basis of N piecewise-affine nodal hat functions $\phi_{i,k} : M \to \mathbb{R}$ are defined with $x_{i,k}$ the node of the i^{th} hat function. The function $\phi_{i,k}$ is locally supported on mesh elements with $x_{i,k}$ as a vertex and $\phi_{i,k}(x_{i,k}) = 1$. The usual stiffness and mass matrices are computed on each mesh and averaged across time.

$$D = \frac{1}{n}\sum_{k=1}^{n} D_k, \qquad D_{k,lm} = \int_{\Phi(M,t;t_k-t)} \nabla\phi_{l,k} \cdot \nabla\phi_{m,k} \tag{11}$$

$$M = \frac{1}{n}\sum_{k=1}^{n} M_k, \qquad M_{k,lm} = \int_{\Phi(M,t;t_k-t)} \phi_{l,k} \cdot \phi_{m,k} \tag{12}$$

The discrete representation of the eigenproblem $\Delta^D_{[t,t+\tau]} f = \lambda f$ is $Dv = \lambda M v$, which is immediately solved in e.g. MATLAB. The approximate solution f is then recovered as $f = \sum_{i=1}^{N} v_i \phi_{i,1}$. An example computation is shown in Fig. 15 for the dominant 17 eigenfunctions.

4.1 Disentangling Multiple Features with SEBA

In both the transfer operator approach of Sect. 3.2 and the dynamic Laplace approach considered here, it is frequently the case that multiple finite-time coherent sets are encoded in several dominant approximate singular vectors of $\mathbf{L}_{t,\tau,\epsilon}$ and eigenfunctions of $\Delta^D_{[t,t+\tau]}$, respectively. This is illustrated in Fig. 15 for the 17 dominant eigenfunctions of $\Delta^D_{[t,t+\tau]}$. In order to disentangle individual finite-time coherent sets, we seek a rotation of the eigendata so that each rotated vector contains a single set. We use sparsity as the means to drive the rotation towards this individual feature separation, because sparse[2] vectors imply a small total feature support in each vector. In more detail, if each singular vector or eigenvector $v^b, b = 1, \ldots, B$ is a column vector in $\mathbb{R}^N$ and $V := [v^1|v^2|\cdots|v^B]$ is an $N \times B$ array, we wish to find a sparse array $S = [s^1|s^2|\cdots|s^B]$ for which $\text{span}\{s^1, s^2, \ldots, s^B\} \approx \text{span}\{v^1, v^2, \ldots, v^B\}$. This is carried out using the SEBA (Sparse EigenBasis Approximation) algorithm [51], which finds a locally optimal $B \times B$ rotation matrix R with $V \approx SR$ small and S sparse; see Sect. 3 [51] for further details. Figure 16 shows the conversion of the eigenbasis displayed

[2] A sparse vector (resp. array) is a vector (resp. array) with a high proportion of zero elements.

in Fig. 15 to a new approximate sparse eigenbasis, with each vector isolating a single feature. The same approach is employed in the three-dimensional results in Fig. 18.

5 Application to Rayleigh-Bénard Convection

Turbulent convection flows in nature are often organized in regular large-scale patterns which evolve gradually compared to the typical convective time unit and arranged on spatial scales which are much larger than the layer height H. Prominent examples are cloud streets in atmospheric or granulation and supergranulation patterns in solar convection. This order in a fully developed turbulent flow is termed *turbulent superstructure of convection* in the following. Pandey et al. [47] reported their appearance in turbulent RBC flows with very different molecular dissipation properties which are characterized by the dimensionless Prandtl number Pr. A second dimensionless parameter of RBC which measures the vigor of convective turbulence is the Rayleigh number Ra. They are defined as

$$\mathrm{Ra} = \frac{\alpha g \Delta T H^3}{\nu \kappa}, \tag{13}$$

$$\mathrm{Pr} = \frac{\nu}{\kappa}, \tag{14}$$

where α, ν, and κ are the isobaric expansion coefficient, the kinematic viscosity, and the thermal diffusivity of the fluid, respectively. The wall-to-wall temperature difference is given by $\Delta T = T_{\mathrm{bottom}} - T_{\mathrm{top}}$. The acceleration vector due to gravity is given by $\boldsymbol{g} = (0, 0, -g)$. The Prandtl number is extremely small in stellar or solar convection with $\mathrm{Pr} \lesssim 10^{-6}$; it is $\mathrm{Pr} \approx 0.7$ for atmospheric turbulence, and $\mathrm{Pr} \approx 7$ for convective motion in the oceans. The large-scale structure formation in turbulent RBC became recently accessible in direct numerical simulations (DNS), which can now resolve all involved scales of turbulence in simulations in horizontally extended domains with a large aspect ratio [42–45].

Here, we study RBC in two different settings. Our first setting is a two-dimensional DNS of a RBC system with a larger Prandtl number $\mathrm{Pr} = 10$ close to convection in water at a small aspect ratio of $\Gamma = 4$ as in [49]. We restrict here to a two-dimensional model as it has been previously shown that for large Prandtl numbers the large- and small-scale quantities show similar scalings in two- and three-dimensional systems. The second setting is a DNS of three-dimensional RBC with a smaller Prandtl number $\mathrm{Pr} = 0.7$ corresponding to convection in air at a larger aspect ratio of $\Gamma = 16$ as in [48].

5.1 2D System

We consider the same two-dimensional RBC system as in [49], given in the Boussinesq approximation [41], in non-dimensional form by

$$\frac{\partial \boldsymbol{u}}{\partial t} + \boldsymbol{u} \cdot \boldsymbol{\nabla} \boldsymbol{u} = -\nabla p + T \boldsymbol{e}_z + \sqrt{\frac{\mathrm{Pr}}{\mathrm{Ra}}} \boldsymbol{\nabla}^2 \boldsymbol{u}, \tag{15}$$

$$\frac{\partial \theta}{\partial t} + \boldsymbol{u} \cdot \boldsymbol{\nabla} \theta = u_z + \frac{1}{\sqrt{\mathrm{PrRa}}} \boldsymbol{\nabla}^2 \theta, \tag{16}$$

$$\boldsymbol{\nabla} \cdot \boldsymbol{u} = 0, \tag{17}$$

where $\boldsymbol{u} = (u_x, u_z)$, θ, and p are the velocity, temperature fluctuation, and pressure fluctuation fields, respectively. The temperature fluctuations θ are deviations from the linear conductive (equilibrium) profile and related to the total temperature field T via

$$T(x, z, t) = T_{\mathrm{bottom}} - \frac{\Delta T}{H} z + \theta(x, z, t), \tag{18}$$

where T_{bottom} is the temperature at the bottom plate. Equations (15–17) are nondimensionalized using the height H of the convective layer as the length scale, the free-fall velocity $u_f = \sqrt{\alpha g \Delta T H}$ as the velocity scale, and the temperature difference ΔT as the temperature scale. Stress-free boundary conditions for the velocity field are applied at all walls. The side walls have Neumann boundary conditions, $\partial T / \partial n = 0$. Top and bottom walls are held at constant temperatures (as already mentioned before). Consequently, $\theta = 0$ at the top and bottom. Equations (15–17) are solved for $\mathrm{Pr} = 10$ and $\mathrm{Ra} = 10^6$ in a two-dimensional box of aspect ratio $\Gamma = L_x / H = 4$ subject to appropriate boundary conditions. The computational details are described in [49].

We start our simulation with random velocity and temperature fields as the initial condition and continued until a statistically steady state is reached. The steady state flow structure exhibits a pair of counter-rotating circulation rolls. Hot fluid rises in the central region whereas cold fluid falls near the sidewalls. The velocity and temperature fields at all the grid points were written to output files at every $0.1\, t_f$, with $t_f = H / u_f$ being the free-fall time (which is taken as the convective time unit).

The flow map required for setting up the transition matrix P is obtained from numerical advection of massless particles with coordinates $\boldsymbol{x}$ in the computed velocity field corresponding to

$$\frac{d\boldsymbol{x}}{dt} = \boldsymbol{u}(\boldsymbol{x}, t). \tag{19}$$

Time integration is done by the RK4 method and spatial interpolation of the velocities by cubic splines.

We consider a box covering $\{B_1, \ldots, B_n\}$ of the simulation domain $X = [0, 4] \times [0, 1]$ by 2^{12} or 2^{16} square boxes. As the system is closed we can choose $Y = X$ and thus use the same box covering for the initial and the final time.

For the computation of the transition matrix a 4×4 uniform grid of test points is initialized in each box B_i and advected by the flow map $\Phi(\cdot, 2000; \tau)$. As in [49] we consider the two different cases $\tau = 20t_f$ and $\tau = 200t_f$. Note that the average turnover time for a tracer is $20t_f$ for this setting [49].

In the following, we will compare different Lagrangian methods for coherent sets in the two-dimensional flow at hand. These are finite-time entropy (FTE), finite time Lyapunov exponents (FTLE), transfer operator method, and the sparse eigenbasis approximation (SEBA).

5.1.1 Short Flow Time $\tau = 20$

In order to visualize the major transport barrier separating the two convection roles, we compute the forward time FTE field from P as described in Sect. 3.3. As shown in Fig. 1, the FTE field has large values in the box center where hot fluid rises and also at the boundaries, where cold fluid falls, and thus where the main heat transport takes place. This result is in agreement with the computed FTLE field shown in Fig. 2.

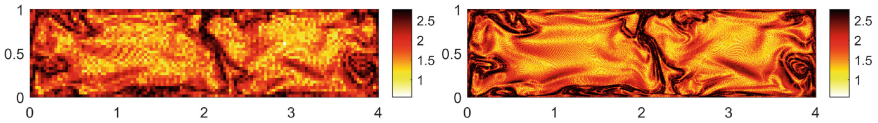

Fig. 1. FTE fields $FTE(\cdot, 2000; 20)$ computed over the time interval $[2000, 2020]$ and plotted with respect to initial positions for two different box coverings (left: 2^{12} boxes; right: 2^{16} boxes). Dark regions are characterized by large stretching and correspond to dominant transport barriers.

For the extraction of coherent sets, we compute the leading left and right singular vectors as described in Sect. 3.2 for the coarse (Fig. 3) and the finer box discretization (Fig. 4). The second singular vectors identify the left-right division induced by the major transport barrier and highlight the two different gyres (Figs. 3 and 4, left columns). The third singular vectors (right columns) distinguish the two gyre cores from the background flow. Further singular vectors (not shown) subdivide the gyre cores into smaller structures. This has also been

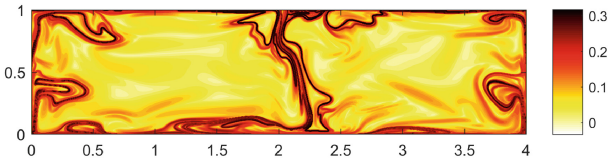

Fig. 2. FTLE field $FTLE(\cdot, 2000; 20)$ computed over the time interval $[2000, 2020]$. As in Fig. 1 dark regions correspond to dominant transport barriers.

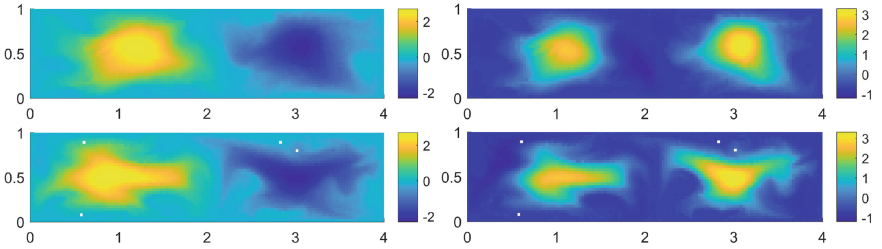

Fig. 3. Left singular vectors $\mathbf{w}_2$ and $\mathbf{w}_3$ (top row) and corresponding right singular vectors $\hat{\mathbf{w}}_2$ and $\hat{\mathbf{w}}_3$ (bottom row) obtained from the modified transition matrix (9) highlight coherent sets at initial and final time of the computation over the short time interval $[2000, 2020]$. Here 2^{12} boxes are used for setting up the transition matrix.

observed in [49]. The results for the two different box coverings are very similar, indicating that the computational results are very robust.

There are spectral gaps after the second singular values in both settings. However, in order to extract the apparently three dominant coherent sets (two gyres and background) from the leading singular vectors, we apply a standard k-means algorithm to the three leading left singular vectors. The results for both box coverings, which are again very similar, are shown in Fig. 5. This approach separates the two gyre cores from the background flow, where most of the heat transport takes place.

As an alternative to the hard-clustering resulting from k-means, we aim to find a sparse basis representation of the space spanned by the leading three singular vectors. Using SEBA [51] as briefly explained at the end of Sect. 4, two of the resulting sparse vectors are supported on each the gyre cores (Fig. 6, top), and the third sparse vector is supported on the background flow region (Fig. 6, bottom, left). A superposition of the three vectors (Fig. 6, bottom, right) reveals in dark blue a particularly incoherent (well mixing) region separating the two

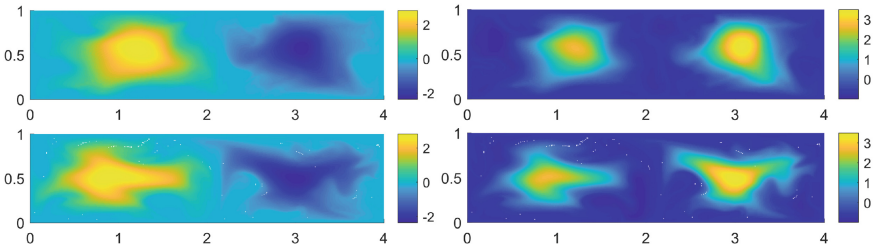

Fig. 4. Left singular vectors $\mathbf{w}_2$ and $\mathbf{w}_3$ (top row) and corresponding right singular vectors $\hat{\mathbf{w}}_2$ and $\hat{\mathbf{w}}_3$ (bottom row) obtained from the modified transition matrix (9) highlight coherent sets at initial and final time of the computation over the short time interval $[2000, 2020]$. Here 2^{16} boxes are used for setting up the transition matrix.

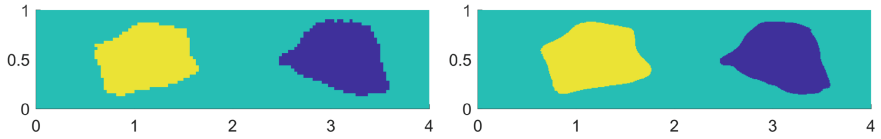

Fig. 5. Extracted coherent sets via an application of the standard k-means algorithm on the first three left singular vectors based discretizations with 2^{12} boxes (left) and 2^{16} boxes (right) for the short time interval $[2000, 2020]$.

gyres from the background flow. We note that the results are comparable to those in [49].

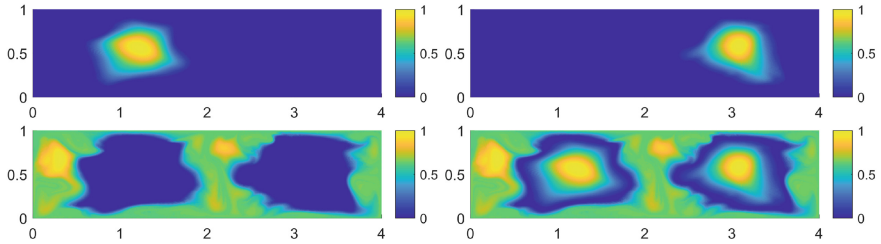

Fig. 6. SEBA applied to the first three left singular vectors, 2^{16} boxes, time interval $[2000, 2020]$. The upper row shows two of the output sparse vectors. Lower left shows the third output sparse vector and lower right shows the superposition of the three sparse vectors, revealing an incoherent region in dark blue.

5.1.2 Long Flow Time $\tau = 200$

For the long flow time $\tau = 200$ we have studied again the system using the coarse and the fine box covering. As these results are again very similar, we will show only the results for the finer box covering of 2^{16} boxes.

The FTE field (Fig. 7) highlights extended regions of strong stretching, which fill the space apart from the gyre cores, which appear to have decreased in size considerably and have developed into more filamentary shapes. This is confirmed by the FTLE field shown in Fig. 8.

The shrinking and filamentation of the gyre cores is also observed in the leading left and right singular vectors (Fig. 9). While the second singular vectors (left column) are analogous to those of the short time study, the third singular vector (right column) appears to further subdivide the right gyre. This has also been observed in our previous studies [49].

As there is a spectral gap after the fourth singular value, we use the corresponding four leading left singular vectors for postprocessing. Applying k-means (Fig. 10, left) and SEBA (Fig. 10, right) results in the identification of three very small gyre cores and the background flow.

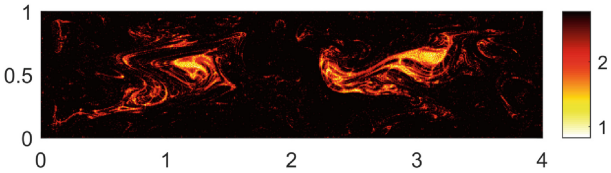

Fig. 7. Forward time FTE field computed over the long time interval $[2000, 2200]$ and plotted with respect to initial positions for a box covering consisting of 2^{16} boxes. Dark regions are characterized by large stretching and correspond to dominant transport barriers.

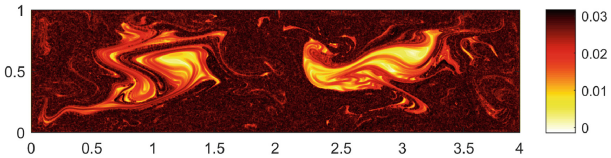

Fig. 8. FTLE field computed over the long time interval $[2000, 2200]$. Dark regions are characterized by large stretching and correspond to dominant transport barriers.

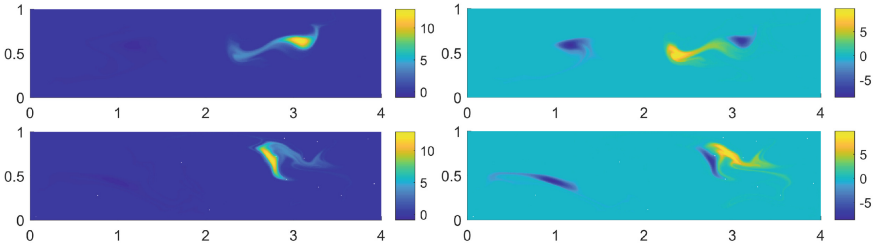

Fig. 9. Left singular vectors $\mathbf{w}_2$ and $\mathbf{w}_3$ (top row) and corresponding right singular vectors $\hat{\mathbf{w}}_2$ and $\hat{\mathbf{w}}_3$ (bottom row) obtained from the modified transition matrix (9) highlight coherent sets at initial and final time of the computation over the long time interval $[2000, 2200]$. Here 2^{16} boxes are used for setting up the transition matrix.

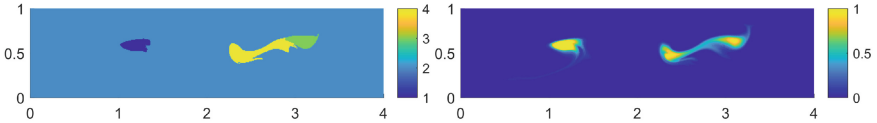

Fig. 10. Extracted coherent sets from the leading four left singular vectors for the long time interval $[2000, 2200]$ via k-means (left) and SEBA (right).

5.2 3D System

Here, we solve the three-dimensional version of RBC which is again given in dimensionless form by Eqs. (15–17). No-slip boundary conditions for the velocity field $\boldsymbol{u} = (u_x, u_y, u_z)$ are applied at all walls, i.e., $\boldsymbol{u} = 0$. The side walls are again thermally insulated, i.e., Neumann boundary conditions $\partial T/\partial n = 0$ are applied. At the top and bottom walls, a constant dimensionless temperature of $T = 0$ and 1 is maintained again. Following ref. [48], we solve these equations numerically for $Ra = 10^5$ and $Pr = 0.7$ in a closed three dimensional box of aspect ratio $\Gamma = L_x/H = L_y/H = 16$, i.e. $M = [-8, 8] \times [-8, 8] \times [0, 1]$. For more details on the DNS we refer to [48]. During the simulation, the trajectories required for setting up the transition matrix are approximated. For this 512^2 points (tracers are initialized on a regular grid at a height of $z = 0.03$ above the bottom plate which is well inside the thermal boundary layer δ_T (that has a mean thickness of about 0.12). The tracers are advected by a 3-step explicit Adams-Bashforth scheme. The interpolation of the velocity field is done spectrally.

5.2.1 Quasi-2D Set-Oriented Study

As the convection cell is very flat ($\Gamma \gg 1$) the large-scale structures are expected to be arranged in horizontal patterns. This is clearly visible in the time-averaged temperature fields, see Fig. 11. We therefore restrict to a quasi-two-dimensional set-oriented study and take the temperature field in the midplane as the reference. As discussed in [47], an average of T at a given time t with respect to the vertical coordinate z would provide basically the same information. Note also that RBC has a statistical up-down reflection symmetry with respect to the midplane. Thus for the set-oriented approximation of the transfer operator we consider the domain $X = [-8, 8] \times [-8, 8]$ and ignore the vertical coordinate. We subdivide X into 2^{14} equally sized square boxes, hence each box contains 16 uniformly distributed test points initially. We set up the transition matrices corresponding to three different flow times $t = 2.6, 5.2, 10.5 t_f$. We also incorporate a small amount of explicit diffusion as the dynamics is very dissipative at the beginning. Note that the flow times are short in comparison to the average turnover time of a tracer in the layer. This time is on average $t \approx 19 t_f$ for this parameter setting [48].

At the beginning of the simulation, the tracers are attracted to the regions where the hot fluid rises from the bottom to the top of the convection cell, which correspond to attracting sets, at least on a finite-time span. We first study this particular behavior by means of the FTE field, see Fig. 12 and compare with Fig. 11. Regions of strong stretching are observed which appear to bound the different basins of attraction. Note that these basins can be related to a pair of convection rolls. In particular, the FTE field for flow time $5.2 t_f$ compares very nicely to the time-averaged temperature fields in Fig. 11. For longer flow times the picture becomes increasingly fuzzy due to turbulent dispersion. The same behavior was also observed for the FTLE field in previous work [48], see also Fig. 13.

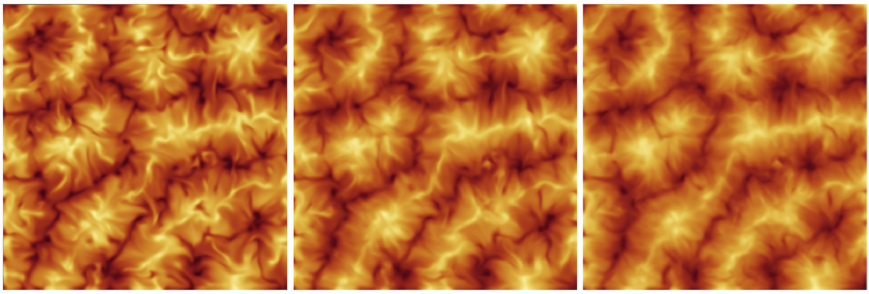

Fig. 11. Time-averaged temperature fields at mid-plane for different time spans $2.6, 5.2, 10.5t_f$. Light regions correspond to hot rising fluid, dark areas to cold descending fluid.

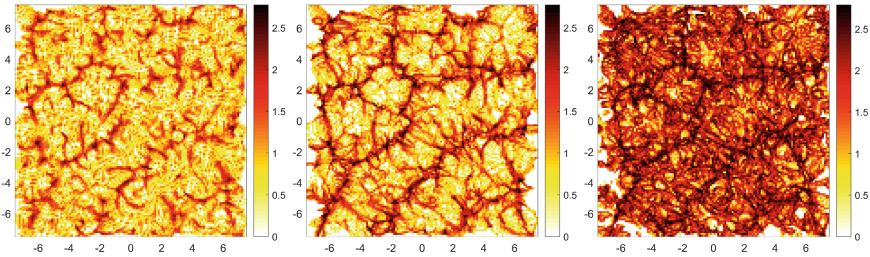

Fig. 12. FTE fields obtained from the transition matrices for flow times $2.6, 5.2, 10.5t_f$. Dark colors indicate to regions of strong stretching, which compare well with the structures formed by descending cold fluid in Fig. 11.

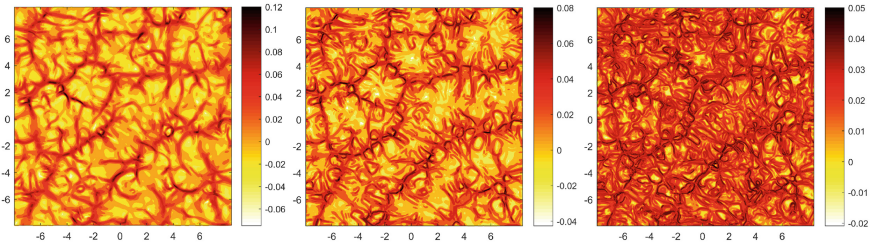

Fig. 13. FTLE fields for flow times $2.6, 5.2, 10.5t_f$. Dark colors indicate to regions of strong stretching, which compare well with the structures formed by descending cold fluid in Fig. 11 and also with the corresponding FTE fields in Fig. 12.

We also extract coherent sets based from the numerical transfer operator for the three different time spans. After inspecting the spectra we use the 13 leading left singular vectors for the settings with flow times $2.6t_f$ and $5.2t_f$ and 19 for the longer flow time. The results after a k-means postprocessing are shown in Fig. 14. The results for the two smaller flow times are very similar and compare again well to the temperature contours in Fig. 11. In particular, coherent sets

appear to be made up of pairs of convection roles. The picture becomes more fuzzy for flow time $10.5t_f$ due to turbulent dispersion. The results compare well to our previous data-based studies in [48].

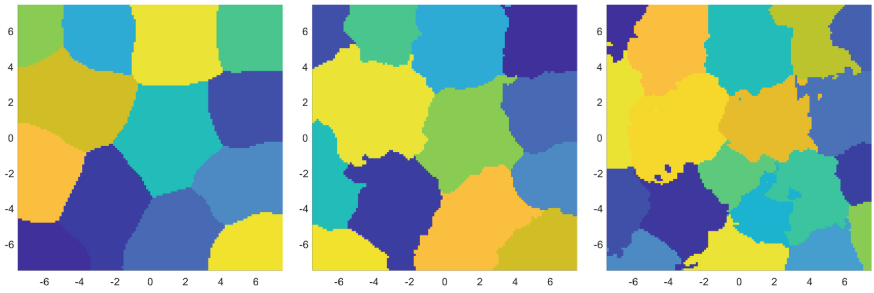

Fig. 14. Coherent sets extracted from the leading left singular vectors of the corresponding transition matrices for the three different flow times using k-means clustering. 13 clusters are obtained for flow times $2.6t_f$ (left) and $5.2t_f$ (middle), and 19 clusters for the long flow time $10.5t_f$ (right).

5.2.2 3D Finite-Element Study

For the remaining experiments we populate the entire three-dimensional domain with test points distributed throughout the domain. Further, we reduce the number of test points by more than six-fold to 40,000 and employ the dynamic Laplace approach of Sect. 4.

Before presenting the fully three-dimensional results, we remove the z-coordinate and investigate the flow for the longest time duration of $10.5t_f$. Triangulating the 40,000 points creates meshes of around 80,000 triangles; we compute the matrices D and M from (11) and (12) and solve the eigenproblem $Dv = \lambda Mv$. Using SEBA and the sparse vector heuristic in Sect. 4.2.2 [51], we choose 17 eigenvectors as a strong local minimum of the envelope produced by the MATLAB function `MinValStackedPlot.m` in Appendix A.6 [51], and illustrated in Fig. 11 [51]. Figure 15 shows the first 17 eigenfunctions of the dynamic Laplacian. These dominant 17 eigenvectors are input to SEBA in order to extract 17 individual coherent features. These 17 sparse vectors, representing the likelihoods of points belonging to individual coherent sets, are shown in Fig. 16. Maxima of the likelihoods can be plotted to create a single "hot-spot" image, and hard thresholded; see Fig. 17.

We now include the z-coordinate and begin our fully three-dimensional experiments. The 40,000 points are meshed into around 265,000 tetrahedra, and the matrices D and M are computed using the three-dimensional version of FEMDL (see [31] and http://github.com/gaioguy/FEMDL for examples and code). We again look for local minima in the `MinValStackedPlot.m` output and for visualisation purposes, choose a slightly smaller number of vectors, namely we use the most robust 10 SEBA vectors from the most dominant 12 eigenvectors. As in Fig. 16, each of the 10 vectors provides a pointwise likelihood that a point belongs

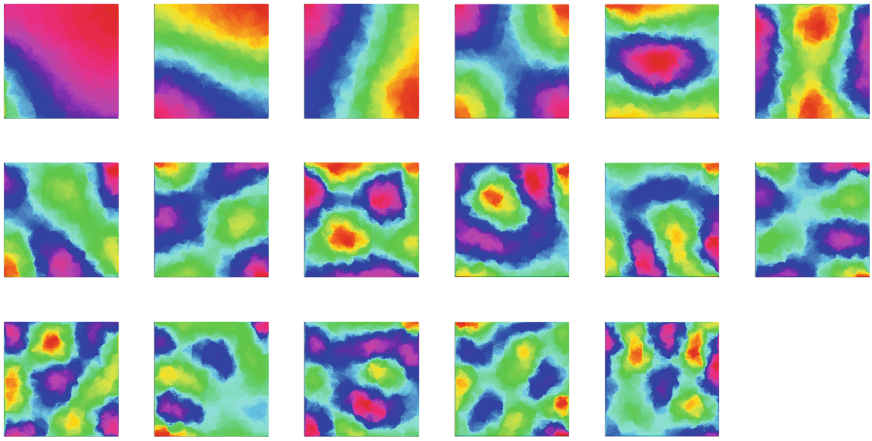

Fig. 15. Dominant 17 eigenvectors of the dynamic Laplacian for flow time $10.5t_f$. The colourmap is chosen so that bright pink and red values are extreme values that correspond to coherent features.

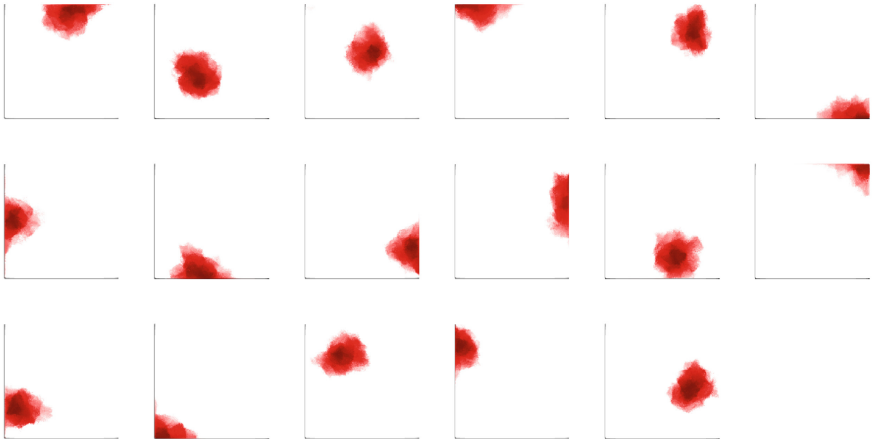

Fig. 16. Output of SEBA applied to the 17 dominant eigenvectors shown in Fig. 15. Negative parts have been removed. The colour scale ranges from 0 (white) to 1 (red); the intensity of red indicates the likelihood that a point belongs to each individual coherent feature.

to a particular coherent set. To clearly visualise these 10 three-dimensional coherent sets, we plot the isosurface[3] at value 1/2. As the likelihood increases toward the centre of the sets (we verified this visually, not shown), one can interpret

[3] Recall a SEBA vector defines a continuous, piecewise-linear function, affine on each tetrahedron. MATLAB's isosurface function requires a regular grid, so we reinterpolate to approximately the same number of points and the approximately the same density on a regular $80 \times 80 \times 10$ grid.

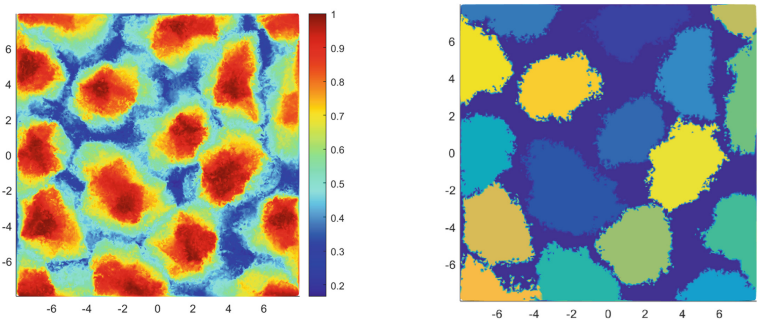

Fig. 17. Left: Maximum of intensities of individual SEBA vectors shown in Fig. 16, representing total probability to belong to one of the 17 identified coherent sets. Right: Maximum likelihood coherent sets created from the left image.

these surfaces as containing all points that are more than 50% likely to belong to each coherent set; one could call them the "cores" of the coherent sets. Figure 18 upper left shows the 10 three-dimensional cores. Note that each of these cores extends almost all of the way from the bottom to the top of the domain, consistent with the overall nature of the flow, where fluid mostly rises from the bottom of the domain to the top, before overturning and heading back toward the bottom of the domain. This full vertical extent feature is extremely robust to the number of eigenvectors and SEBA vectors used. Figure 18 lower left displays the same image as the upper left, but with commensurate lengths, emphasising that the domain is much shorter in the vertical direction. Figure 18 right is again the

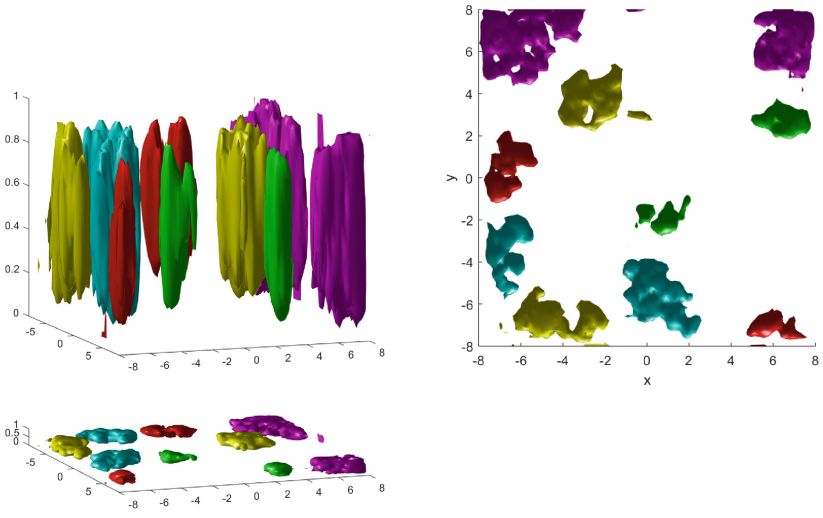

Fig. 18. Cores of 10 three-dimensional coherent sets for flow time $10.5t_f$.

same image, but viewing directly from above. Figure 18 displays cores roughly of the same size, and in some cases in similar locations, as the coherent sets in Fig. 17, although with fewer plotted for clearer three-dimensional visualisation.

6 Conclusion and Outlook

In this work, we have applied transfer operator based numerical frameworks for analyzing coherent behavior in nonautonomous systems to Rayleigh-Bénard convection in two- and three-dimensional settings. To this end, we used set-oriented approximations of the transfer operator and finite-element approximations of the dynamic Laplacian. It turns out that these general frameworks reliably identify the core regions of the various convection rolls as the regions that contribute least to the turbulent heat transfer from the bottom to the top. The two-dimensional results compare well with those of previous studies [48,49]. Future work will address the long-term evolution of the turbulent superstructures of convection and as well as their impact on transport properties.

Acknowledgements. KPG is thankful for the many fruitful discussions with Michael Dellnitz over the past more than twenty years. His fundamental contributions to the transfer operator based analysis of transport processes in dynamical systems have had a huge impact on the development of the overall field and on her own research. GF thanks Michael Dellnitz for countless stimulating mathematical discussions, for introducing him to the idea of almost-invariant sets, and for introducing him to his German colleagues in the late 90s, many of whom remain collaborators (and friends). Michael Dellnitz has also been one of the drivers of the Priority Programme SPP 1881 Turbulent Superstructures of the Deutsche Forschungsgemeinschaft by which the present work is supported and the authors are grateful for this. GF additionally thanks Universities Australia and the DAAD for a joint research travel grant, which partially supported his visit to Germany.

References

1. Allshouse, M.R., Peacock, T.: Lagrangian based methods for coherent structure detection. Chaos **25**, 097617 (2015)
2. Hadjighasem, A., Farazmand, M., Blazevski, D., Froyland, G., Haller, G.: A critical comparison of Lagrangian methods for coherent structure detection. Chaos **27**, 053104 (2017)
3. Kreuzer, E.: Numerische Untersuchung nichtlinearer dynamischer Systeme. Springer (1987)
4. Hsu, C.S.: Cell-to-Cell Mapping: A Method of Global Analysis for Nonlinear Systems. Springer, New York (1987)
5. Dellnitz, M., Hohmann, A.: A subdivision algorithm for the computation of unstable manifolds and global attractors. Numer. Math. **75**, 293–317 (1997)
6. Dellnitz, M., Junge, O.: Almost invariant sets in Chua's circuit. Int. J. Bifurc. Chaos **7**, 2475–2485 (1997)
7. Dellnitz, M., Junge, O.: On the approximation of complicated dynamical behaviour. SIAM J. Numer. Anal. **36**(2), 491–515 (1999)

8. Froyland, G.: Statistically optimal almost-invariant sets. Physica D **200**, 205–219 (2005)
9. Froyland, G., Padberg, K.: Almost-invariant sets and invariant manifolds - connecting probabilistic and geometric descriptions of coherent structures in flows. Physica D **238**, 1507–1523 (2009)
10. Froyland, G., Junge, O., Koltai, P.: Estimating long-term behavior of flows without trajectory integration: the infinitesimal generator approach. SIAM J. Numer. Anal. **51**, 223–247 (2013)
11. Ulam, S.: Problems in Modern Mathematics. Wiley, New York (1964)
12. Li, T.Y.: Finite approximation for the Frobenius-Perron operator. A solution to Ulam's conjecture. J. Approx. Theory **17**, 177–186 (1976)
13. Deuflhard, P., Dellnitz, M., Junge, O., Schütte, C.: Computation of essential molecular dynamics by subdivision techniques. In: Deuflhard, P., Hermans, J., Leimkuhler, B., Mark, A.E., Reich, S., Skeel, R.D. (eds.) Computational Molecular Dynamics: Challenges, Methods, Ideas, pp. 98–115. Springer, Heidelberg (1999)
14. Schütte, C., Huisinga, W., Deuflhard, P.: Transfer operator approach to conformational dynamics in biomolecular systems. In: Fiedler, B. (ed.) Ergodic Theory, Analysis, and Efficient Simulation of Dynamical Systems, pp. 191–223. Springer, Heidelberg (2001)
15. Dellnitz, M., Junge, O., Koon, W., Lekien, F., Lo, M., Marsden, J., Padberg, K., Preis, R., Ross, S., Thiere, B.: Transport in dynamical astronomy and multibody problems. Int. J. Bifurc. Chaos **15**, 699–727 (2005)
16. Dellnitz, M., Junge, O., Lo, M.W., Marsden, J.E., Padberg, K., Preis, R., Ross, S.D., Thiere, B.: Transport of Mars-crossing asteroids from the quasi-Hilda region. Phys. Rev. Lett. **94**, 231102 (2005)
17. Froyland, G., Padberg, K., England, M.H., Treguier, A.M.: Detection of coherent oceanic structures via transfer operators. Phys. Rev. Lett. **98**, 224503 (2007)
18. Dellnitz, M., Froyland, G., Horenkamp, C., Padberg-Gehle, K., Sen Gupta, A.: Seasonal variability of the subpolar gyres in the Southern Ocean: a numerical investigation based on transfer operators. Nonlinear Process. Geophys. **16**, 655–663 (2009)
19. Neumann, N., Goldschmidt, S., Wallaschek, J.: On the application of set-oriented numerical methods in the analysis of railway vehicle dynamics. Proc. Appl. Math. Mech. **4**, 578–579 (2004)
20. Froyland, G., Stuart, R.M., van Sebille, E.: How well connected is the surface of the global ocean? Chaos **24**, 033126 (2014)
21. Koltai, P.: A stochastic approach for computing the domain of attraction without trajectory simulation. Discrete Contin. Dyn. Syst. Suppl. **2011**, 854–863 (2011)
22. Froyland, G., Lloyd, S., Santitissadeekorn, N.: Coherent sets for nonautonomous dynamical systems. Physica D **239**, 1527–1541 (2010)
23. Froyland, G., Santitissadeekorn, N., Monahan, A.: Transport in time-dependent dynamical systems: finite-time coherent sets. Chaos **20**, 043116 (2010)
24. Froyland, G.: An analytic framework for identifying finite-time coherent sets in time-dependent dynamical systems. Physica D **250**, 1–19 (2013)
25. Froyland, G., Padberg-Gehle, K.: Almost-invariant and finite-time coherent sets: directionality, duration, and diffusion. In: Bahsoun, W., Bose, C., Froyland, G. (eds.) Ergodic Theory, Open Dynamics, and Coherent Structures, pp. 171–216. Springer, Heidelberg (2014)
26. Dellnitz, M., Horenkamp, C.: The efficient approximation of coherent pairs in non-autonomous dynamical system. Discrete Contin. Dyn. Syst. A **32**, 3029–3042 (2012)

27. Denner, A., Junge, O., Matthes, D.: Computing coherent sets using the Fokker-Planck equation. J. Comput. Dyn. **3**, 3–18 (2016)
28. Froyland, G., Koltai, P.: Estimating long-term behavior of periodically driven flows without trajectory integration. Nonlinearity **30**, 1948 (2017)
29. Froyland, G., Koltai, P., Plonka, M.: Computation and optimal perturbation of finite-time coherent sets for aperiodic flows without trajectory integration. *arXiv preprint* arXiv:1902.09263 (2019)
30. Froyland, G.: Dynamic isoperimetry and the geometry of Lagrangian coherent structures. Nonlinearity **28**, 3587 (2015)
31. Froyland, G., Junge, O.: Robust FEM-based extraction of finite-time coherent sets using scattered, sparse, and incomplete trajectories. SIAM J. Appl. Dyn. Syst. **17**, 1891–1924 (2018)
32. Froyland, G., Padberg-Gehle, K.: A rough-and-ready cluster-based approach for extracting finite-time coherent sets from sparse and incomplete trajectory data. Chaos **25**, 087406 (2015)
33. Hadjighasem, A., Karrasch, D., Teramoto, H., Haller, G.: Spectral-clustering approach to Lagrangian vortex detection. Phys. Rev. E **93**, 063107 (2016)
34. Schlueter-Kuck, K.L., Dabiri, J.O.: Coherent structure colouring: identification of coherent structures from sparse data using graph theory. J. Fluid Mech. **811**, 468 (2017)
35. Banisch, R., Koltai, P.: Understanding the geometry of transport: diffusion maps for Lagrangian trajectory data unravel coherent sets. Chaos **27**, 035804 (2017)
36. Padberg-Gehle, K., Schneide, C.: Network-based study of Lagrangian transport and mixing. Nonlinear Process. Geophys. **24**, 661 (2017)
37. Pierrehumbert, R.T., Yang, H.: Global chaotic mixing on isentropic surfaces. J. Atmos. Sci. **50**, 2462–2480 (1993)
38. Haller, G.: Lagrangian coherent structures. Ann. Rev. Fluid Mech. **47**, 137 (2015)
39. Froyland, G., Padberg-Gehle, K.: Finite-time entropy: a probabilistic approach for measuring nonlinear stretching. Physica D **241**, 1612–1628 (2012)
40. Padberg, K., Thiere, B., Preis, R., Dellnitz, M.: Local expansion concepts for detecting transport barriers in dynamical systems. Commun. Nonlinear Sci. Numer. Simul. **14**, 4176–4190 (2009)
41. Chillà, F., Schumacher, J.: New perspectives in turbulent Rayleigh-Bénard convection. Eur. Phys. J. E **35**, 58 (2012)
42. Hartlep, T., Tilgner, A., Busse, F.H.: Large scale structures in Rayleigh-Bénard convection at high Rayleigh numbers. Phys. Rev. Lett. **91**, 064501 (2003)
43. von Hardenberg, J., Parodi, A., Passoni, G., Provenzale, A., Spiegel, E.A.: Large-scale patterns in Rayleigh-Bénard convection. Phys. Lett. A **372**, 2223 (2008)
44. Bailon-Cuba, J., Emran, M.S., Schumacher, J.: Aspect ratio dependence of heat transfer and large-scale flow in turbulent convection. J. Fluid Mech. **655**, 152 (2010)
45. Emran, M.S., Schumacher, J.: Large-scale mean patterns in turbulent convection. J. Fluid Mech. **776**, 96 (2015)
46. Stevens, R.A.J.M., Blass, A., Zhu, X., Verzicco, R., Lohse, D.: Turbulent thermal superstructures in Rayleigh-Bénard convection. Phys. Rev. Fluids **3**, 041501(R) (2018)
47. Pandey, A., Scheel, J.D., Schumacher, J.: Turbulent superstructures in Rayleigh-Bénard convection. Nat. Commun. **9**, 2118 (2018)
48. Schneide, C., Pandey, A., Padberg-Gehle, K., Schumacher, J.: Probing turbulent superstructures in Rayleigh-Bénard convection by Lagrangian trajectory clusters. Phys. Rev. Fluids **3**, 113501 (2018)

49. Schneide, C., Stahn, M., Pandey, A., Junge, O., Koltai, P., Padberg-Gehle, K., Schumacher, J.: Lagrangian coherent sets in turbulent Rayleigh-Bénard convection. Phys. Rev. E **100**, 053103 (2019)
50. Dellnitz, M., Froyland, G., Junge, O.: The algorithms behind GAIO - set oriented numerical methods for dynamical systems. In: Fiedler, B. (ed.) Ergodic Theory, Analysis, and Efficient Simulation of Dynamical Systems, pp. 145–174. Springer, Heidelberg (2001)
51. Froyland, G., Rock, C.P., Sakellariou, K.: Sparse eigenbasis approximation: multiple feature extraction across spatiotemporal scales with application to coherent set identification. Commun. Nonlinear Sci. Numer. Simul. **77**, 81–107 (2019)